Iterative Adaptive Sparse Sampling Method for Magnetic Resonance Imaging

Giuseppe Placidi[1], Luigi Cinque[2], Andrea Petracca[1], Matteo Polsinelli[1] and Matteo Spezialetti[1]
[1]*A[2]VILab, Department of Life, Health & Environmental Sciences, University of L'Aquila, Via Vetoio, L'Aquila, Italy*
[2]*Department of Computer Science, Sapienza University, Via Salaria, Rome, Italy*
giuseppe.placidi@univaq.it, cinque@di.uniroma1.it, andrea.petracca@graduate.univaq.it, matteo.polsinelli@student.univaq.it, matteo.spezialetti@graduate.univaq.it

Keywords: Adaptive Acquisition Method, Sparse Sampling, Compressed Sensing, Undersampling, Sparsity, Reconstruction, Radial Directions, Projections, Non-linear Reconstruction.

Abstract: Magnetic Resonance Imaging (MRI) represents a major imaging modality for its low invasiveness and for its property to be used in real-time and functional applications. The acquisition of radial directions is often used but a complete examination always requires long acquisition times. The only way to reduce acquisition time is undersampling. We present an iterative adaptive acquisition method (AAM) for radial sampling/reconstruction MRI that uses the information collected during the sequential acquisition process on the inherent structure of the underlying image for calculating the following most informative directions. A full description of AAM is furnished and some experimental results are reported; a comparison between AAM and weighted compressed sensing (CS) strategy is performed on numerical data. The results demonstrate that AAM converges faster than CS and that it has a good termination criterion for the acquisition process.

1 INTRODUCTION

Magnetic Resonance Imaging (MRI) is a major non-invasive imaging modality, due to its ability to provide anatomical details and information on physiological status and pathologies. The reconstruction of a single image usually involves the acquisition of a series of trajectories. The measurement of a trajectory is a sampling process of a function evolving with time in a domain referred to as *k*-space. Raw data are then used to reconstruct the images (O'Sullivan, 1985; Jackson et al., 1991). The most popular k-space trajectories are straight lines on a Cartesian grid, in which each k-space line corresponds to the frequency encoding readout at each value of the phase encoding gradient (Spin Warp Imaging, (Edelstein et al., 1980)). The lines in the grid are parallel and equally separated. Although the acquisition of Cartesian trajectories allows easier image reconstruction, recent advances in MRI hardware allow other acquisition patterns, such as spirals (Meyer, 1998), radial trajectories (Projection Reconstruction, PR (Lauterbur, 1973)) and other curve trajectories (Placidi, 2010). PR, in particular, is fundamental for real time and functional MRI applications because it reduces the effects due to motion and improves the signal to noise ratio (SNR) in the reconstructed image (the center of k-space is oversampled). In these applications, the gain in the reconstructed images, both in artifacts reduction and in improvement of functional information, is proportional to the time saved during acquisition.

The acquisition process for MRI can be defined by the following linear system:

$$y = Ax + z \tag{1}$$

where y are the linear measurements of a h dimensional vector in the k-space, A is an hxM matrix of h directions, x is the unknown MxM image and z is a Gaussian noise added to the measurements.

A fundamental limitation of MRI is the linear relation between the number of acquired trajectories and net scan time (Eq. 1): minutes are often required to collect a complete data set. Such duration can be too high when dynamic processes have to be observed at high temporal resolution, as for example in functional studies (Bernstein et al., 2004). Moreover, the image quality can be lowered by the presence of movement artifacts intrinsic to the observed dynamic process. The acquisition time for each trajectory is limited by the slow natural relaxation times which are beyond the control of the acquisition sequence and have to be waited. The only way to speed up acquisition is

Placidi, G., Cinque, L., Petracca, A., Polsinelli, M. and Spezialetti, M.
Iterative Adaptive Sparse Sampling Method for Magnetic Resonance Imaging.
DOI: 10.5220/0006199105100518
In *Proceedings of the 6th International Conference on Pattern Recognition Applications and Methods (ICPRAM 2017)*, pages 510-518
ISBN: 978-989-758-222-6

to reduce the number of trajectories, that is by using undersampling. Undersampling is the violation of the Nyquists criterion where images are reconstructed by using a smaller number of samples than what is theoretically required to obtain a fully sampled image. One of these methods (Placidi et al., 2000) presented a *k*-space adaptive acquisition technique that calculated the information content of the collected projections to drive the measurements of the following projections. Modified Fourier reconstruction algorithm, including an interpolation method (Placidi et al., 1998; Placidi and Sotgiu, 2004), were used to reconstruct the image from the resulting sparse set of projections. The same algorithm was also used in the field of image compressing (Placidi, 2009a). Other authors (Candes et al., 2006; Donoho, 2006) presented the theory of Compressed Sensing (CS) and the details of its implementation for rapid MRI (Lustig et al., 2007). CS allows accurate reconstruction of images with far fewer measurements than traditional methods, when two requirements are met: sparsity and incoherence. Sparsity means that the image information can be represented, in some domain, using a small number of coefficients without compromising the image quality. Incoherence implies that the energy of objects in the sparse domain is spread out in the measurement domain. CS in MRI typically uses wavelet transform to promote sparsity and random k-space sampling to ensure incoherence. If sparsity and incoherence are satisfied, an image can be recovered to high accuracy, even if k-space is significantly undersampled, by solving the following convex optimization:

$$min_x \|\Psi x\|_1 : \|y - \Phi x\| \leq \varepsilon, \qquad (2)$$

Here, y are the acquired *k*-space samples in the Fourier Space, Φ is the Fourier transform and Ψ is a transform where the image is sparse (wavelet transform is used therein), and ε is a threshold level that bounds the noise.

Most of the CS applications used the l_1-norm minimization as reconstruction method. Reconstruction can also be improved by increasing samples in the central part of the k-space, because low frequency terms contain more energy than high frequency terms, as demonstrated in weighed CS (Wang and Arce, 2010; Magnusson et al., 2010). In (Arias-Castro et al., 2013) the authors discussed the limits of any adaptive sensing technique with respect to the classical CS scheme in the sense that, if we have a number of measurements sufficiently high (this "sufficiently high" number is very hard to estimate when nothing is known about the underlying image), the error obtained by classical CS acquisition/reconstruction process is almost equivalent to that obtained by a "smart" adaptive acquisition/reconstruction method. Though this is right, it has been shown elsewhere (Placidi et al., 2000; Placidi et al., 2014; Placidi, 2014; Ciancarella et al., 2012; Placidi, 2009b) that it may be possible to reduce the minimum number of necessary projections (Brooks and Di Chiro, 1976), if information about sample internal symmetries and shape can be collected during acquisition. These methods, though very effective in reducing acquisition time while obtaining high quality images, are not optimal in the estimation of the image sparsity value and require highly specialized software (dedicated hardware is also recommended). We present a simple iterative adaptive sparse acquisition strategy for radial (PR) sampling/reconstruction MRI that uses the inherent structure of the underlying image for obtaining an efficient adaptive acquisition method (AAM). In what follows, a full description of AAM is furnished and some experimental results are reported; a comparison between the proposed technique and weighted CS is performed on numerical data. The main advantages of AAM with respect to weighted CS are that its estimation error could converge faster than CS and that AAM detailed an accurate estimate of the sparsity value of the underlying image, that is a good termination criterion for the acquisition process.

2 MATERIALS AND METHODS

The proposed AAM is a variant of a deterministic acquisition method (ADM) or CS strategy, with the advantage of eliminating the blind phase during the acquisition process by using a choice mechanism to select the acquisition trajectories that are most "informative", basing on the shape of the underlying image (Figure 1).

AAM is an iterative process that analyses the data acquired during the sequential acquisition phase in order to obtain useful information regarding the following most "informative" directions to be explored: the process is adaptive in the sense that it adapts the following directions to the shape of the object under investigation. The information regarding the shape of the object are collected starting by an initial subset of the possible directions and used to reconstruct an approximation of the object. The following refinements are obtained by integrating the initial set with other directions collected where highest is the information content.

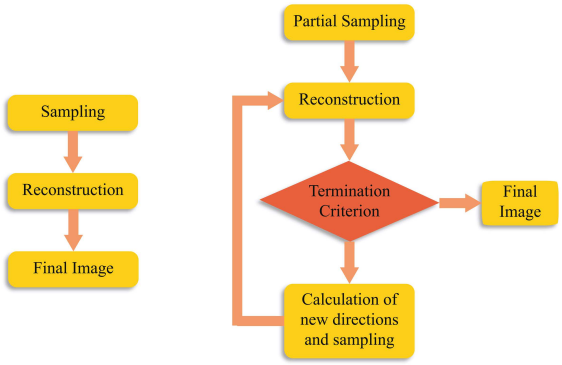

Figure 1: AAM (right) is different with respect to ADM or CS (left) because ADM and CS use a pre-determined set of regular (ADM) or random directions (CS) while AAM uses the information collected during the previous acquisition steps for the calculation of the following directions where the information content is maximum. Moreover AAM is adaptive with respect to the shape of the unknown image and it contains a termination criterion to stop acquisition when the resulting image has reached the maximum quality.

2.1 Relationship between an Image and Its Wavelet e Fourier Domains

The use of wavelets in MRI is not new: examples can be found in (Sung and Hargreaves, 2013; Chen and Huang, 2012).

Since data in MRI are collected in the k-space (the Fourier domain), the relationship between the Fourier and Wavelet domains of a give image, well described in (Sung and Hargreaves, 2013; Gonzalez and Woods, 2007), can be used. This relationship allows to separate the k-space in different regions corresponding to different Wavelet subbands.

In fact, given an image, its Fourier and Wavelet transforms are related as shown in Figure 2. The approximation image in the wavelet domain (right part of the figure, higher left square) has a Fourier transform that corresponds to the central window of the Fourier coefficients of the complete image (left part of the figure, central square). Analogously, the wavelet coefficients of the details (in red, blue and brown coloured regions) have their correspondence in the regions indicated on the left with the same combination of colors.

Figure 2 directly correlates the coloured subbands to the regions with the same colors in the *k*-space, each wavelet level corresponding to a specific Fourier frame.

The previous relationship can be used to reformulate the reconstruction problem of Eq. 2 as follows (see Figure 2 for convenience):

$$min_w \|w\|_1 : \|y - \Phi\Psi^{-1}w\| \leq \varepsilon. \quad (3)$$

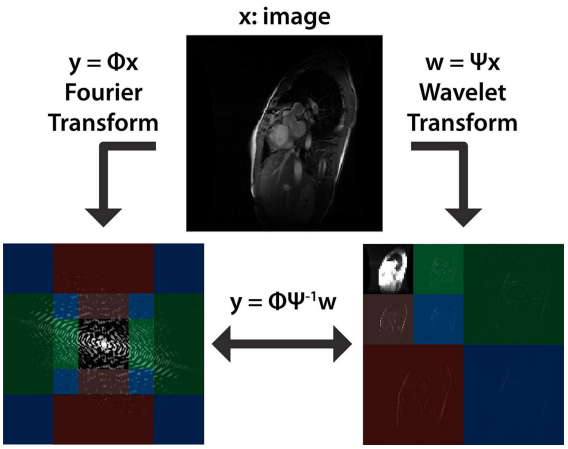

Figure 2: Relationship between image domains: x=image space, y=Fourier space, w=Wavelet space.

In this case, the matrix A in Eq. 1 is $A = \Phi\Psi^{-1}\Psi = \Phi$. The problem can be interpreted as to find x such that x is sparse in the Wavelet domain ($\Psi x = w$) and that its representation in the Fourier domain ($\Phi\Psi^{-1}w = \Phi x$) is very close to what has been acquired ($\Phi x = y$).

A is the matrix connecting the two domains: one, the Fourier domain, in which data are collected and the other, the Wavelet domain, necessary to promote sparsity.

2.1.1 Upsampling in the Wavelet Domain

The previous relationship can be used for reconstruction purposes (Sung and Hargreaves, 2013) but, more importantly for our problem, also for acquisition purposes, that is to drive the acquisition process towards the most informative regions of the image wavelet space and, hence, of the Fourier space.

It is important to note that in Figure 3 the central region of the *k*-space represents an approximation of the complete image.

For example, by considering the image of size MxM (M=256) in Figure 3, if we select a square of Fourier coefficients around the *k*-space center of size $\frac{M}{2}$x$\frac{M}{2}$ and use these data to reconstruct the image (through FFT), the resulting image will have half resolution of the original image but the shape of the image is still well recognizable. What has been lost are the horizontal, vertical and diagonal details that are described by the excluded high frequency coefficients (region external to the red square in Figure 3).

Since the selected approximation maintains most of the features of the original image, it can be argued that there is a strict correlation between the completely sampled image and each of its approximations, to any level (the correlation is greater for levels closer to the considered approximation).

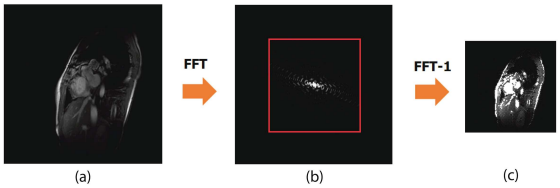

Figure 3: (a) Original 256x256 image; (b) *k*-space representation with a selected central region of size 128x128; (c) Reconstructed 128x128 image obtained by Fourier transforming the selected *k*-space region.

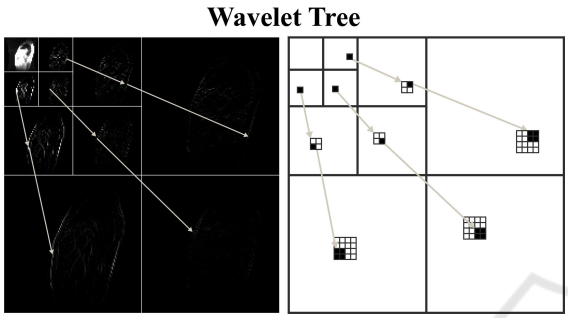

Figure 4: Wavelet coefficients tree structure. In the left panel, the wavelet transform of a real image is shown; in the right panel, the corresponding scheme is reported by using an inverted color palette, for convenience.

Such correlation is codified in the wavelet domain with a tree structure existing between the different levels of each component (see Figure 4). If relevant information are present on the root, it is highly probable that relevant information are present also at the details levels. This correlation can be used also in the negative case: if relevant information are absent on the root, it is highly probable that they will be absent also at the details levels. This property can be used to compress the image: set 0 the details deriving from an irrelevant root coefficient. This tree structure is defined *quadtree* (Sung and Hargreaves, 2013). A *quadtree* is a tree of positions in which, starting from a root $[i, j]$, its child are positioned at $[2i, 2j]$, $[2i+1, 2j]$, $[2i, 2j+1]$, $[2i+1, 2j+1]$.

By knowing the position of an irrelevant (respectively, relevant) wavelet coefficient at a root of a *quadtree* we can assume information regarding the irrelevance of all its descendants in the tree (respectively, we can define a further wavelet decomposition of the current root image and, by using the correlation between the new root and its child, it is possible to estimate the details at finer scales, that is to interpolate). If we iterate this process, we can reach the original image details, as described below.

2.2 The Proposed Method

AAM is an iterative method that uses the relationship between the collected data in the *k*-space, the image space and the wavelet space, as reported in the flowchart of Figure 5.

In this case, the wavelet space is used as a support space for its good properties of multiresolution (it is simple and effective to estimate image details starting from its raw approximation, without producing aliasing) and locality (errors due to estimation are confined around the point in which they were produced, not affecting the whole image). In words (see Figures 5 and 6), AAM starts by considering a subset of equispaced radial directions: for the given dataset, would exist a reduced square support in the Fourier space for which the resulting image is fully sampled (square n.1 in Figure 6). Then, for this support the image is reconstructed. If the maximum image support is reached, the process is terminated and the reconstructed image is the final image. Otherwise, the wavelet transform of the image is calculated and the horizontal, vertical and diagonal details are estimated: the image is upsampled of a factor of 2 in the wavelet domain. Then, the inverse wavelet transform is calculated and finally the inverse Fourier transform of the resulting image is performed. In this case, a Fourier support double than the previous is obtained for the unknown image (square n.2 in Figure 6). At this step, the mean power spectrum is calculated for each circular segment (circular segments are comprised between circles n.1 and n.2 and separated by contiguous radial directions in Figure 6) and the vector E, containing the mean power spectrum values, is ordered in descending order. As long as $max(E) > \varepsilon$ (ε is a power spectrum threshold that will be defined below), repeat the measurement of a new radial direction between the two directions where $max(E)$ is present, update the E values and reorder them in a descending order. Return to the "SET DIM VALUE" point in Figure 5. It is important to note that, during the intermediate steps, the newly collected radial directions cover the whole image support and not just the current reduced square.

2.2.1 Acquisition Parameters

The user-defined parameters are, in this case, two: the number of equispaced radial directions to start the acquisition process that, implicitly, depends on the size of the *k*-space support of the first approximation image (square n.1 in Figure 6); the ε value corresponding to the noise level, the same used in the reconstruction process (Eq. 2) as a termination parameter. Both these parameters can be simply calculated. In fact, the first approximation support is $M/8$ (the size of square n.1

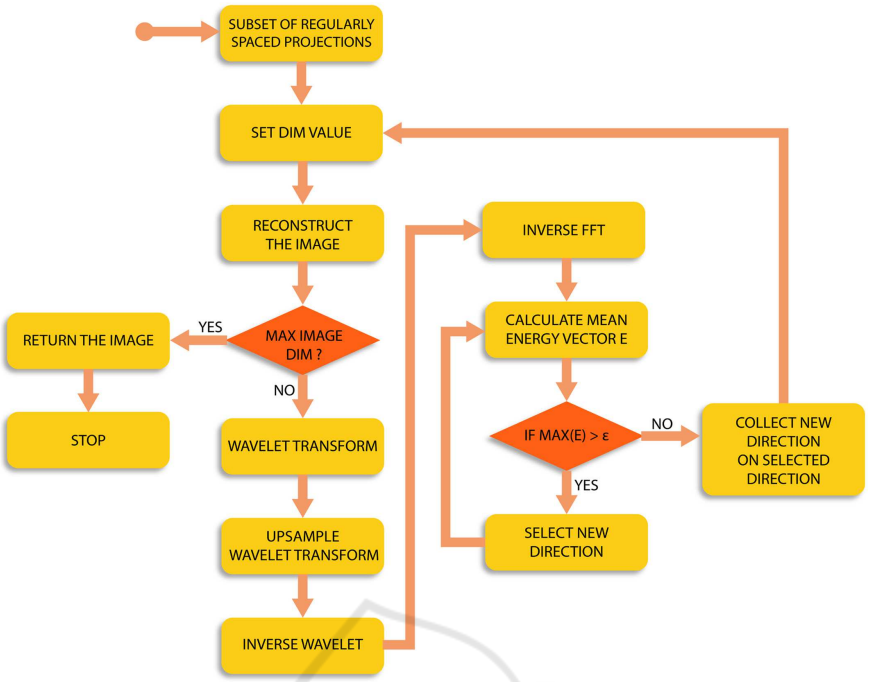

Figure 5: Flow-chart of the AAM.

in Figure 6), having considered M as a power of two (intrinsic MRI resolution usually implies $M = 256$). In this case, having supposed each radial direction is sampled on M points (each with $M/8$ points on circle n.1 in Figure 6), the number of equally spaced radial directions m_0 to fill uniquely the circle n.1 in Figure 6 is about $m_0 \cong \frac{\pi r^2}{p_d}$ (the area of a circle calculated as the number of pixels contained inside it divided by the number of samples of each radial direction falling inside the circle) where $r = M/16$ is the circle radius in pixels and $p_d = M/8$ is the number of points of each radial direction falling inside the circle (Brooks and Di Chiro, 1976; Placidi et al., 1995)). In our case, having considered images where $M = 256$ and a first approximation support of $M/8 = 32$, it follows that $r = 16$, $p_d = 32$ and $m_0 = 26$. The second parameter, ε, represent the noise level, the mean power spectrum level of the noise (Placidi et al., 2000):

$$\varepsilon = \frac{1}{s}\sum_{i=1}^{s}(R_i^2 + I_i^2), \tag{4}$$

in which s is the number of samples of different radial directions falling outside the circle n.4, where just noise is present because out the image support and R_i and I_i are the real and imaginary components of each data sample, respectively. These data are collected when the first set of radial directions is measured by prolonging the measurement of each direction: the time used does imply no wast of time because it uses

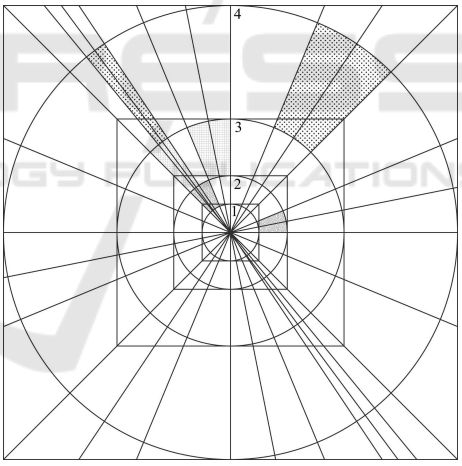

Figure 6: AAM operative example. The highlighted circular segments represent those where higher is the mean power and a new radial direction is collected.

the temporal interval necessary to recover the spin magnetization (Placidi, 2012).

3 EXPERIMENTS

Simulations are performed on cardiac MRI completely sampled 4D data, from a dataset of 240 images (image size 256x256 pixels, 65.536 samples) consisting of 20 temporal frames (*time*=1,...,20) and 12 *x-y*

slices along the *z* axis (*depth*=1,...,12).

To perform the tests, full acquisitions are simulated through the Fourier transform of completely reconstructed images. In this way the complete datasets of the *k*-space samples are assumed. In order to simulate undersampled acquisitions, binary masks, containing "1" where the coefficients have to be collected and "0" where the coefficients have to be discarded, are multiplied, point by point, with the complete datasets.

This operation, though does not reflect precisely a real experimental process (phase errors, off-resonance effects, thermal instability, etc., are not considered), is useful for having a complete reference image that can be used to estimate the performance AAM in terms of Mean Square Error (MSE) with respect the fully sampled. In this way, a wrong reconstruction can only be due to a wrong sampling/reconstruction method and not also to other experimental factors.

The images obtained with AAM are compared with those of a weighted CS, in which a double random acquisition along cartesian directions, rows/columns, is performed by using a normalised Gaussian weighted function with $\mu = 0$ (0 indicates that the mean value is in the *k*-space center) and $\sigma = 1$ (1 indicates a distance equal to 64 rows/columns from the center): this weight is chosen to prefer the *k*-space central area where the image power is higher with respect to the peripheral zones.

The CS sampling/reconstruction process, being a single step reconstruction, is performed by changing the number of rows and columns (the number of rows is equal to the number of columns). The dataset starts from 7000 samples with increments of 5.000 samples, until an almost completely sampled image is reached. It is important to note that for each dataset the acquisition process restarts from the beginning, without increasing the dataset collected in the previous steps.

The starting value for the weighted CS (7.000 samples) is completely arbitrary and it is just used to compare the CS results with the starting dataset used for the AAM (that equals to 6656 samples, being the result of 26 starting projections each containing 256 sampled). The sequence of AAM images are obtained by adding, at each step of the algorithm, the new directions adaptively selected: the dataset grows by adding new directions to those previously collected.

The resulting image, both for the CS and for all the steps of AAM, is obtained by using the l_1-norm minimization.

The tests are executed in MatLab R2015a (http://www.mathworks.com) on a workstation equipped with operating system Windows 7, a processor Intel (R) Core (TM) I7-6700 (3.40 Ghz), 16 GB of RAM and an SSD drive.

Aim of the performed simulations is to show that AAM is really able to identify/collect the most informative directions by comparing its results with CS, used for reference. Moreover, it is also useful to verify the AAM stopping criterion and its good capability in estimating the sparsity value of the underlying image. The tests have been conducted on the whole dataset of 240 images but the results are shown just for a single image, being the others very similar (the images have similar shape and support, especially those allowing to the same time instant). The details of the tests, performed with the image $z = 1$ and time 3 (Figure 7), are reported in Figure 8 where the MSE is calculated for each of the intermediate reconstructions. Figure 9 and Figure 10 show the conservation of the image wavelet coefficients for an intermediate reconstruction both for AAM (intermediate reconstruction with 11520 collected samples) and CS (17000 samples).

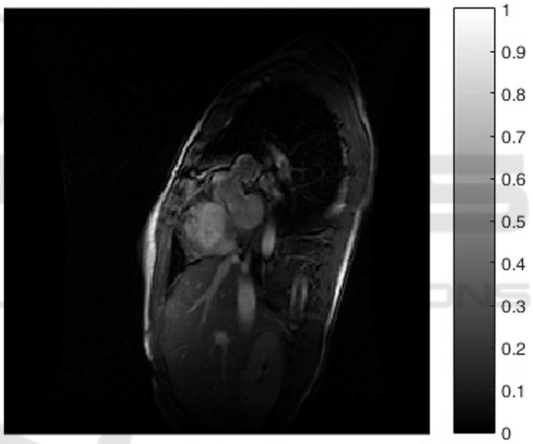

Figure 7: One of the test images: z=1, time=3.

In particular, it can be noted that for AAM most of the wavelet coefficients correspond to those of the original image (wrongly placed or missing coefficients are very few, as indicated by the red zones in Figure 9); on the contrary, for the CS image most of the wavelet coefficients are wrongly placed (artifacts are evident outside the image support in the wavelet image) or lost (red zones in Figure 10).

This is also confirmed by corresponding MSE values (Figure 8): the MSE for the AAM intermediate reconstruction is about one order of magnitude lower than that of CS, though by using a lower number of samples. From Figure 8, it is very interesting to note that the MSE values for AAM is constantly descendent while this does not occur for CS (the CS dataset, being re-sampled, could encounter "unfortunate" directions); moreover, the MSE of AAM is constantly

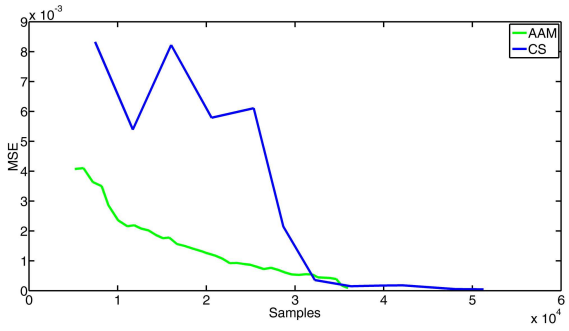

Figure 8: Calculated MSE for intermediate reconstructions of AAM (green line) and for CS (blue line).

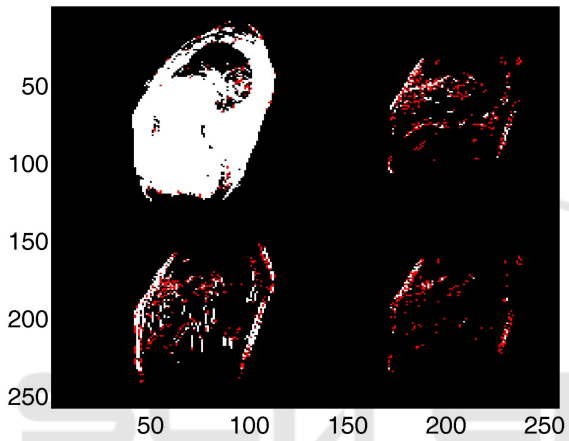

Figure 9: Wavelet correspondences between AAM intermediate reconstruction with 11520 samples and the fully sampled image. White are the correctly placed coefficients. Red are the missing or wrongly placed coefficients with respect to the original image.

below that of CS (CS converges to that of AAM when a high number of samples is used).

On the contrary, the termination criterion used for AAM allows to stop the acquisition process when the MSE becomes plateful (92 directions with 23552 coefficients were used). The calculated value is a good approximation of the sparsity value of the original image. In fact, by performing the wavelet transformation of the original image with a threshold on the noise level, the calculated sparsity value is 18170. The same MSE value is reached by CS at 32000, about 29% more samples than those necessary for AAM. Moreover, CS requires to go over 32000 in order to reduce the probability of a wrong reconstruction, since it has no way to know in advance the sparsity of the underlying image. The results obtained for the whole image dataset are summarized in Figure 11). As can be observed: 1) the MSE values obtained with the AAM method are very close to, in some cases also better than, those obtained by CS, though the images are obtained with less than 60% of the coefficients used

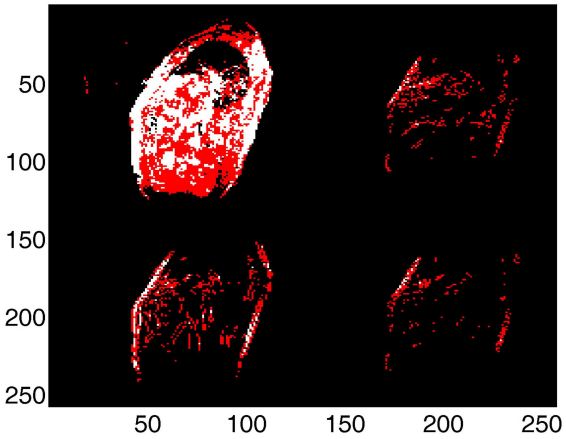

Figure 10: Wavelet correspondences between CS reconstruction with 17000 samples and the fully sampled image. White are the correctly placed coefficients. Red are the missing or wrongly placed coefficients with respect to the original image.

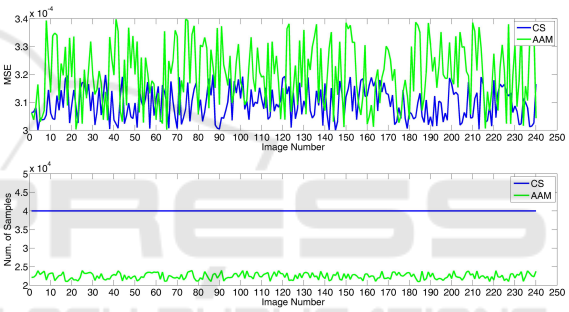

Figure 11: Calculated MSE (up) and final number of samples (down) used for AAM (green line) and CS (blue line) reconstructions of each image composing the dataset. The number of samples for CS is always 40000.

for CS; 2) for CS a fixed number of 40000 samples are used since it does not use the sparsity of the image; 3) the number of coefficients calculated by AAM slightly oscillates around 22000, having the images of the dataset very similar shape (heart moves and changes but chest and lungs structures remain almost unchanged).

4 CONCLUSIONS

We have presented an iterative adaptive acquisition method for radial sampling/reconstruction in MRI that uses the information on the inherent structure of the underlying image collected during the sequential acquisition process for calculating the following most informative directions. The method has been described and some experimental results reported. A comparison between the proposed method and a

weighted compressed sensing strategy was performed on a cardiac MRI examination composed by 240 images. The images were compared both visually and through the MSE evaluation with respect to the completely sampled version of each image. The results demonstrated that AAM converged faster than CS by using just the necessary coefficients (about 55% of those used by CS). Future research will be spent for evaluating the performance of AAM with respect to other adaptive acquisition schemes.

ACKNOWLEDGEMENTS

The Authors are grateful to Mrs Carmelita Marinelli for technical assistance.

REFERENCES

Arias-Castro, E., Candes, E., and Davenport, M. (2013). On the fundamental limits of adaptive sensing. *IEEE Transactions on Information Theory*, 59(1):472–481.

Bernstein, M., King, K., and Zhou, X. (2004). *Handbook of MRI Pulse Sequences*. Elsevier Academic Press.

Brooks, R. and Di Chiro, G. (1976). Principles of computer assisted tomography (cat) in radiographic and radioisotopic imaging. *Physics in Medicine and Biology*, 21(5):689–732.

Candes, E., Romberg, J., and Tao, T. (2006). Robust uncertainty principles: exact signal reconstruction from highly incomplete frequency information. *IEEE Transactions on Information Theory*, 52(2):489–509.

Chen, C. and Huang, J. (2012). Compressive sensing mri with wavelet tree sparsity. In *Advances in Neural Information Processing Systems*, pages 1124–1132.

Ciancarella, L., Avola, D., Marcucci, E., and Placidi, G. (2012). A hibrid sampling strategy for sparse magnetic resonance imaging. In *Computational Modelling of Objects Represented in Images. Fundamentals, Methods and Applications*, pages 285–289, Boca Raton – USA. CRC Press, Taylor & Francis Group.

Donoho, D. (2006). Compressed sensing. *IEEE Transactions On Information Theory*, 52(4):1289–1306.

Edelstein, W., Hutchison, J., Johnson, G., and Redpath, T. (1980). Spin warp nmr imaging and applications to human whole-body imaging. *Physics in Medicine and Biology*, 25(4):751–756.

Gonzalez, R. and Woods, R. (2007). *Digital Image Processing (3rd Edition)*. Pearson.

Jackson, J., Meyer, C., Nishimura, D., and Macovski, A. (1991). Selection of a convolution function for fourier inversion using gridding [computerised tomography application]. *IEEE Transactions on Medical Imaging*, 10(3):473–478.

Lauterbur, P. (1973). Image formation by induced local interactions: examples employing nuclear magnetic resonance. *Nature*, 242(5394):190–191.

Lustig, M., Donoho, D., and Pauly, J. (2007). Sparse mri: The application of compressed sensing for rapid mr imaging. *Magnetic Resonance in Medicine*, 58(6):1182–1195.

Magnusson, M., Leinhard, O., Brynolfsson, P., Thyr, P., and Lundberg, P. (2010). 3d magnetic resonance imaging of the human brain - novel radial sampling, filtering and reconstruction. In *12th IASTED International Conference on Signal and Image Processing (SIP 2010)*. ACTA Press.

Meyer, C. (1998). *Spiral echo-planar imaging*, pages 633–658. Springer Berlin Heidelberg.

O'Sullivan, J. (1985). A fast sinc function gridding algorithm for fourier inversion in computer tomography. *IEEE Transactions on Medical Imaging*, 4(4):200–207.

Placidi, G. (2009a). Adaptive compression algorithm from projections: Application on medical greyscale images. *Computers in biology and medicine*, 39:993–999.

Placidi, G. (2009b). Constrained reconstruction for sparse magnetic resonance imaging. In *World Congress on Medical Physics and Biomedical Engineering, September 7 - 12, 2009, Munich, Germany*, volume 25/4, pages 89–92, Berlin Heidelberg – DEU. Springer.

Placidi, G. (2010). Circular acquisition to define the minimum set of projections for optimal mri reconstruction. *Lecture notes in computer science*, 6026:254–262.

Placidi, G. (2012). *MRI: essentials for innovative technologies*. CRC Press, Taylor & Francis Group, Boca Raton – USA.

Placidi, G. (2014). Recent advances in acquisition/reconstruction algorithms for undersampled magnetic resonance imaging. *Journal of biomedical engineering and medical imaging*, 1:59–78.

Placidi, G., Alecci, M., Colacicchi, S., and Sotgiu, A. (1998). Fourier reconstruction as a valid alternative to filtered back projection in iterative applications: Implementation of fourier spectral spatial epr imaging. *Journal of Magnetic Resonance*, 134(2):280–286.

Placidi, G., Alecci, M., and Sotgiu, A. (1995). Theory of adaptive acquisition method for image reconstruction from projections and application to epr imaging. *Journal of magnetic resonance. Series A*, 108:50–57.

Placidi, G., Alecci, M., and Sotgiu, A. (2000). Omega-space adaptive acquisition technique for magnetic resonance imaging from projections. *Journal of Magnetic Resonance*, 143(1):197–207.

Placidi, G., Avola, D., Cinque, L., Macchiarelli, G., Petracca, A., and Spezialetti, M. (2014). Adaptive sampling and non linear reconstruction for cardiac magnetic resonance imaging. In *Computational Modeling of Objects Presented in Images Fundamentals, Methods, and Applications*, volume 8641, pages 24–35.

Placidi, G. and Sotgiu, A. (2004). A novel restoration algorithm for reduction of undersampling artefacts

from magnetic resonance images. *Magnetic resonance imaging*, 22:1279–1287.

Sung, K. and Hargreaves, B. (2013). High-frequency subband compressed sensing mri using quadruplet sampling. *Magnetic Resonance in Medicine*, 70(5):1306–1318.

Wang, Z. and Arce, G. (2010). Variable density compressed image sampling. *IEEE Transactions on Image Processing*, 19(1):264–270.